

(CLQCD Collaboration)

**Low-energy Scattering of  $(D^*\bar{D}^*)^\pm$  System and the Resonance-like Structure  $Z_c(4025)$** Ying Chen,<sup>1</sup> Ming Gong,<sup>1</sup> Yu-Hong Lei,<sup>2</sup> Ning Li,<sup>3</sup> Jian Liang,<sup>1</sup> Chuan Liu,<sup>4,5,\*</sup> Jin-Long Liu,<sup>2</sup> Yong-Fu Liu,<sup>2</sup> Yu-Bin Liu,<sup>6</sup> Zhaofeng Liu,<sup>1</sup> Jian-Ping Ma,<sup>7</sup> Zhan-Lin Wang,<sup>2</sup> and Jian-Bo Zhang<sup>8</sup><sup>1</sup>*Institute of High Energy Physics, Chinese Academy of Sciences, Beijing 100049, China*<sup>2</sup>*School of Physics, Peking University, Beijing 100871, China*<sup>3</sup>*School of Science, Xi'an Technological University, Xi'an 710032, China*<sup>4</sup>*School of Physics and Center for High Energy Physics, Peking University, Beijing 100871, China*<sup>5</sup>*Collaborative Innovation Center of Quantum Matter, Beijing 100871, China*<sup>6</sup>*School of Physics, Nankai University, Tianjin 300071, China*<sup>7</sup>*Institute of Theoretical Physics, Chinese Academy of Sciences, Beijing 100190, China*<sup>8</sup>*Department of Physics, Zhejiang University, Hangzhou 311027, China*

In this paper, low-energy scattering of the  $(D^*\bar{D}^*)^\pm$  meson system is studied within Lüscher's finite-size formalism using  $N_f = 2$  twisted mass gauge field configurations. With three different pion mass values, the  $s$ -wave threshold scattering parameters, namely the scattering length  $a_0$  and the effective range  $r_0$ , are extracted in  $J^P = 1^+$  channel. Our results indicate that, in this particular channel, the interaction between the two vector charmed mesons is weakly repulsive in nature hence do not support the possibility of a shallow bound state for the two mesons, at least for the pion mass values being studied. This study provides some useful information on the nature of the newly discovered resonance-like structure  $Z_c(4025)$  observed in various experiments.

**I. INTRODUCTION**

Since the observation of charged charmonium-like structure  $Z_c(3900)$  [1], the BESIII Collaboration studied the process  $e^+e^- \rightarrow \pi^\pm(D^*\bar{D}^*)^\pm$  at a center-of-mass energy of 4.26 GeV and reported a new charged charmonium-like structure which they named as  $Z_c^\pm(4025)$  [2], with a mass of  $4026.3 \pm 2.6 \pm 3.7$  MeV and a width of  $24.8 \pm 5.6 \pm 7.7$  MeV. Such charged charmonium-like states are quite unique in the sense that their valence quark component must contain tetra-quark content  $\bar{q}_1 q_2 \bar{c} c$  where  $q_1$  and  $q_2$  being two different flavors of light quark. Another feature is that, their mass values are rather close to the threshold of two corresponding charmed mesons. It is therefore tempting to explain these new exotic states as shallow bound states of the corresponding mesons. Another explanation is that they are simply genuine tetra-quark hadrons or mixture of the tetra-quark and the two-meson system. Since it is still unclear whether these states are above or below the threshold, it is also possible that they are resonances, or even simply cusp effects due to interaction between different channels. Obviously, a better understanding of the internal structures of these states will provide new insights into the dynamics of multi-quark systems and QCD low-energy behaviors.

The experimental discovery of the charged charmonium-like structures have triggered a lot of theoretical studies in recent years, both using phenomenological methods [3–6] and on the lattice [7, 8].

Since  $Z_c^\pm(4025)$  is near the  $D^*\bar{D}^*$  threshold, a shallow bound state, also known as the molecular state, formed by  $D^*$  and  $\bar{D}^*$  mesons is a possible explanation. To further investigate this possible scenario, the interaction between  $D^*$  and  $\bar{D}^*$  mesons at low-energies becomes important. The energy considered here is very close to the threshold of the  $D^*\bar{D}^*$  system. Therefore the interaction between the charmed mesons is non-perturbative in nature which requires a genuine non-perturbative framework such as lattice QCD.

In this paper, the near-threshold scattering of  $(D^*\bar{D}^*)^\pm$  system is studied using  $N_f = 2$  twisted mass gauge field configurations [9]. The study is carried out for three different values of pion mass corresponding to  $m_\pi = 300, 420, 485$  MeV and the size of the lattices is  $32^3 \times 64$  with a lattice spacing of about 0.067 fm. According to the BESIII results [2], the state  $Z_c(4025)$  is consistent with the quantum number assignment  $J^P = 1^+$  although other assignments are not completely ruled out. Taking into the fact that the state is so close to the threshold where presumably  $s$ -wave scattering will dominate, we will focus on the  $J^P = 1^+$  channel only. Experiments also indicates that the state is strongly coupled to the  $D^*\bar{D}^*$  system. Thus, in this exploratory lattice study, single-channel scattering of a  $D^*$  and a  $\bar{D}^*$  meson is studied using Lüscher's formalism [10]. The  $s$ -wave low-energy scattering parameters, namely the scattering length  $a_0$  and the effective range  $r_0$ , are extracted from our simulation. To enhance the energy resolution close the threshold, twisted boundary conditions are utilized.

This paper is organized as follows. In section II, we briefly recapitulate Lüscher's formalism in general and in the particular case of twisted boundary conditions. Section III defines the one-particle and two-particle interpo-

---

\* Corresponding author. Email: liuchuan@pku.edu.cn

lating operators used in this study and the corresponding correlation functions. In section IV, simulation details are provided and the results for the single-meson and two-meson systems are analyzed. By applying Lüscher's formula, the scattering phases are extracted and when fitted to the known low-energy behavior, the threshold scattering parameters of the system, i.e. the inverse scattering length  $a_0^{-1}$  and the effective range  $r_0$  are obtained. As a crosscheck, both the jackknife and the bootstrap method have been used in this study which yield compatible results. Implications of our results are discussed afterwards. We finally conclude in section V with some general remarks.

## II. THEORETICAL FRAMEWORK

Let us first consider a particle with a mass  $m$  enclosed in a cubic box of size  $L \times L \times L$ , then the ordinary periodic boundary condition in the spatial directions reads

$$\Psi(\mathbf{x} + L\mathbf{e}_i, t) = \Psi(\mathbf{x}, t), \quad (1)$$

with the Cartesian unit vector  $\mathbf{e}_i$  along the  $i$ -th axis ( $i = 1, 2, 3$  for  $x, y, z$  direction). The spatial momentum  $\mathbf{k}$  of this particle is quantized according to:

$$\mathbf{k} = \frac{2\pi}{L} \mathbf{n}, \quad \mathbf{n} \in \mathbb{Z}^3. \quad (2)$$

Now consider two interacting particles with masses  $m_1$  and  $m_2$  in this finite box. Taking the center-of-mass frame of this system, the two particles thus have opposite three-momentum  $\mathbf{k}$  and  $-\mathbf{k}$ . The exact energy  $E_{1,2}$  of the two-particle system is parameterized as

$$E_{1,2}(\mathbf{k}) = \sqrt{m_1^2 + \bar{\mathbf{k}}^2} + \sqrt{m_2^2 + \bar{\mathbf{k}}^2}, \quad (3)$$

where  $\bar{\mathbf{k}}^2$  is a quantity which also encodes the interaction of the two particles in this box. To be specific,  $\bar{\mathbf{k}}^2 = \mathbf{k}^2$  corresponds to the non-interacting case, while  $\bar{\mathbf{k}}^2 > \mathbf{k}^2$  and  $\bar{\mathbf{k}}^2 < \mathbf{k}^2$  corresponds to repulsive or attractive interaction, respectively. Based on Eq. (3), it is more convenient to define a dimensionless quantity  $q^2$ :

$$q^2 = \frac{\bar{\mathbf{k}}^2 L^2}{(2\pi)^2}, \quad (4)$$

such that the repulsive and attractive interactions are translated into  $q^2 > \mathbf{n}^2$  and  $q^2 < \mathbf{n}^2$  for some  $\mathbf{n} \in \mathbb{Z}^3$ , respectively.

In an actual lattice computation, the exact energy  $E_{1,2}$  of the two-particle system hence also the value of  $q^2$  is obtained from corresponding correlation functions. Lüscher's formula relates the value of  $q^2$  and the elastic scattering phase shift  $\delta(q)$  at that particular energy in the infinite volume. In the simplest case of  $s$ -wave elastic scattering, it reads: [10]

$$q \cot \delta_0(q) = \frac{1}{\pi^{3/2}} \mathcal{Z}_{00}(1; q^2), \quad (5)$$

where  $\mathcal{Z}_{00}(1; q^2)$  is the zeta-function which can be evaluated numerically once its argument  $q^2$  is given. Eq. (5) is the main formula to compute the elastic scattering phase shift on the lattice. In the case of attractive interaction, the lowest two-particle energy level can become lower than the threshold. If the interaction is weak, the state is loosely bound, i.e.  $(-q^2)$  being positive but close to zero [11, 12]. However, a negative  $q^2$  value in a finite volume alone does not signifies a bound state. One has to investigate the behavior of the negative energy shift in the large volume limit.

With quantization condition on three-momenta, c.f. Eq. (2), the typical size of the smallest nonzero momentum is still too large to investigate the hadron-hadron near-threshold scattering for practical size of the lattice. We thus utilize the so-called twisted boundary conditions in our study [13, 14]. Following the notation in Ref. [15], the quark field  $\psi_{\boldsymbol{\theta}}(\mathbf{x}, t)$ , when transported by an amount of  $L$  along the spatial direction  $i$  (designated by unit vector  $\mathbf{e}_i$ ,  $i = 1, 2, 3$ ), will acquire an additional phase  $e^{i\theta_i}$ :

$$\psi_{\boldsymbol{\theta}}(\mathbf{x} + L\mathbf{e}_i, t) = e^{i\theta_i} \psi_{\boldsymbol{\theta}}(\mathbf{x}, t), \quad (6)$$

where  $\boldsymbol{\theta} = (\theta_1, \theta_2, \theta_3)$  is the twisted angle (vector) for the quark field in three spatial directions. The conventional periodic boundary conditions corresponds to  $\boldsymbol{\theta} = (0, 0, 0)$ . Twisted boundary conditions such as those in Eq. (6) can be applied to any flavor of quark fields in question. In other words, we are free to choose a twisting angle vector  $\boldsymbol{\theta}_f$  for flavor  $f$ , with  $f = u, d, s, c, \dots$ . Under twisted boundary conditions, the discretized momentum in the finite volume is also modified. So, instead of Eq. (2), we have,

$$\mathbf{p} = \frac{2\pi}{L} \left( \mathbf{n} + \frac{\boldsymbol{\theta}}{2\pi} \right). \quad (7)$$

It is more convenient to introduce the new fields  $\psi'$ , we shall call them the primed fields, via

$$\psi'(\mathbf{x}, t) = e^{-i\boldsymbol{\theta} \cdot \mathbf{x} / L} \psi_{\boldsymbol{\theta}}(\mathbf{x}, t). \quad (8)$$

It is easy to verify that the primed fields  $\psi'(\mathbf{x}, t)$  satisfy the usual periodic boundary conditions, c.f. Eq. (1). For Wilson-type fermions, we can easily calculate the primed quark propagators, which are Wick contractions of the primed fields, using a modified set of gauge fields (the primed gauge fields),  $U'_{x,\mu} = e^{i\theta_\mu a/L} U_{x,\mu}$  with  $\theta_\mu = (0, \boldsymbol{\theta})$  [8, 15].

Traditional meson interpolating operators are constructed using the primed fields as a local bilinears,  $\mathcal{O}_{\Gamma}(\mathbf{x}, t) = \bar{\psi}'_f \Gamma \psi'_{f'}(\mathbf{x}, t)$ , where  $f$  and  $f'$  denoting flavor indices and  $\Gamma$  being a Dirac gamma matrix. By summing over the spatial coordinate  $\mathbf{x}$  with appropriate three-momentum  $\mathbf{p}$ ,

$$\mathcal{O}'_{\Gamma}(\mathbf{p}, t) = \sum_{\mathbf{x}} \bar{\psi}'_f \Gamma \psi'_{f'}(\mathbf{x}, t) e^{-i\mathbf{p} \cdot \mathbf{x}}, \quad (9)$$

one sees that the above operator in fact corresponds to an operator built using the un-primed fields with three momentum:  $\mathbf{p} + (\boldsymbol{\theta}_{f'} - \boldsymbol{\theta}_f)/L$ . Since it is free to choose any

values of  $\theta_f$  and  $\theta_{f'}$ , an improved resolution is achieved in momentum space.

Note that we have adopted twisted boundary conditions for the valence quark fields. This is referred to as the partial twisting. Strictly speaking, the same twisted boundary condition should be applied both to the valence and to the sea quark fields which is called full twisting. It has been shown recently that, in some cases, partial twisting is equivalent to full twisting [16]. In other cases, however, the corrections due to partially twisted boundary conditions are shown to be exponentially suppressed if the size of the box is large [14]. We will assume that these corrections are indeed negligible.<sup>1</sup> In the following calculations, only the light quark fields ( $u$  and  $d$ ) will be twisted while the charm quark fields remain untwisted. This choice carefully avoids potential problems that might have arisen due to annihilation diagrams in this process as suggested in Ref. [16].

### III. OPERATORS AND CORRELATORS

As usual, the energies of single-particle and two-particle systems are obtained from corresponding correlation functions which are measured in our Monte Carlo simulation. Since the newly discovered  $Z_c(4025)$  state is observed in both  $D^*\bar{D}^*$  and the  $h_c\pi$  channel [2], its quantum number is likely to be  $I^G(J^P) = 1^+(1^+)$ . The closeness of its mass to the  $D^*\bar{D}^*$  threshold suggests that it might be a candidate for  $D^*\bar{D}^*$  bound state. In order to investigate the scattering relevant to this scenario on the lattice, we need to construct the  $D^*\bar{D}^*$  two-particle interpolating operators with the right quantum number mentioned above. In practice, for the one-particle operators of  $D^{*\pm}$  and  $\bar{D}^{*0}$ , conventional quark bilinear operators for vector mesons are utilized. The desired two-particle operators for system in the  $I^G(J^P) = 1^+(1^+)$  channel are discussed in the following. Due to the difference in the symmetries, the cases of twisted boundary conditions and non-twisted boundary condition have to be treated somewhat differently.

#### A. Operators in the non-twisted case

Let us first consider the non-twisted case. For a single vector charmed meson and its anti-particle, we utilize the following local interpolating fields in real space:

$$[D^{*+}] : \mathcal{P}_i(\mathbf{x}, t) = [\bar{c}\gamma_i d](\mathbf{x}, t), \quad (10)$$

$$[D^{*-}] : \bar{\mathcal{P}}_i(\mathbf{x}, t) = [\bar{d}\gamma_i c](\mathbf{x}, t) = [\mathcal{P}_i(\mathbf{x}, t)]^\dagger, \quad (11)$$

In the above equation, we have also indicated the quark flavor content of the operator in front of the definition inside the square bracket. So, for example, the operator in Eq. (10) will create a  $D^{*+}$  meson when acting on the QCD vacuum. A single-particle state with definite three-momentum  $\mathbf{k}$  is defined accordingly via usual Fourier transform [17]:

$$\mathcal{P}_i(\mathbf{k}, t) = \sum_{\mathbf{x}} \mathcal{P}_i(\mathbf{x}, t) e^{-i\mathbf{k}\cdot\mathbf{x}}. \quad (12)$$

The conjugate of the above operator is:

$$[\mathcal{P}_i(\mathbf{k}, t)]^\dagger = \sum_{\mathbf{x}} [\mathcal{P}_i(\mathbf{x}, t)]^\dagger e^{+i\mathbf{k}\cdot\mathbf{x}} \equiv \bar{\mathcal{P}}_i(-\mathbf{k}, t). \quad (13)$$

Similarly, for  $\bar{D}^{*0}$  and its anti-particle, we use the following operators:

$$\begin{aligned} [\bar{D}^{*0}] : \mathcal{Q}_i(\mathbf{x}, t) &= [\bar{c}\gamma_i u](\mathbf{x}, t), \\ [D^{*0}] : \bar{\mathcal{Q}}_i(\mathbf{x}, t) &= [\bar{u}\gamma_i c](\mathbf{x}, t) = [\mathcal{Q}_i(\mathbf{x}, t)]^\dagger, \\ \mathcal{Q}_i(\mathbf{k}, t) &= \sum_{\mathbf{x}} \mathcal{Q}_i(\mathbf{x}, t) e^{-i\mathbf{k}\cdot\mathbf{x}}, \\ [\mathcal{Q}_i(\mathbf{k}, t)]^\dagger &= \sum_{\mathbf{x}} [\mathcal{Q}_i(\mathbf{x}, t)]^\dagger e^{+i\mathbf{k}\cdot\mathbf{x}} \equiv \bar{\mathcal{Q}}_i(-\mathbf{k}, t). \end{aligned} \quad (14)$$

For the two-particle operators, in terms of the operators defined above, we have used the following combination for a pair of charmed mesons with back-to-back momentum,

$$\mathcal{P}_i(\mathbf{k}, t) \mathcal{Q}_j(-\mathbf{k}, t) - \mathcal{P}_j(\mathbf{k}, t) \mathcal{Q}_i(-\mathbf{k}, t), \quad (15)$$

with  $i, j = 1, 2, 3$ . On a finite lattice, however, the rotational group  $SO(3)$  is broken down to the cubic group  $O_h$  and  $J^P = 1^+$  of the two-particle system is thus reduced to  $T_1^+$  of the cubic group. To avoid complicated Fierz rearrangement terms, we have put the two mesons on two neighboring time-slices. Thus, we use the following operators to create the state with two charmed mesons,

$$\mathcal{O}^{T_1} \left\{ \begin{aligned} \mathcal{O}_1^{T_1} : & \sum_{R \in G} [\mathcal{P}_2(R \circ \mathbf{k}_\alpha, t+1) \mathcal{Q}_3(-R \circ \mathbf{k}_\alpha, t) \\ & - \mathcal{P}_3(R \circ \mathbf{k}_\alpha, t+1) \mathcal{Q}_2(-R \circ \mathbf{k}_\alpha, t)], \\ \mathcal{O}_2^{T_1} : & \sum_{R \in G} [\mathcal{P}_1(R \circ \mathbf{k}_\alpha, t+1) \mathcal{Q}_3(-R \circ \mathbf{k}_\alpha, t) \\ & - \mathcal{P}_3(R \circ \mathbf{k}_\alpha, t+1) \mathcal{Q}_1(-R \circ \mathbf{k}_\alpha, t)], \\ \mathcal{O}_3^{T_1} : & \sum_{R \in G} [\mathcal{P}_1(R \circ \mathbf{k}_\alpha, t+1) \mathcal{Q}_2(-R \circ \mathbf{k}_\alpha, t) \\ & - \mathcal{P}_2(R \circ \mathbf{k}_\alpha, t+1) \mathcal{Q}_1(-R \circ \mathbf{k}_\alpha, t)], \end{aligned} \right. \quad (16)$$

where  $\mathbf{k}_\alpha$  is a chosen three-momentum mode. The index  $\alpha$  ( $\alpha = 1, \dots, N$ ) denotes the momentum mode considered in our calculation. In this particular case, we have  $N = 4$ . In the above equation,  $G = O_h$  designates the cubic group and  $R \in G$  is an element of the group and we have used the notation  $R \circ \mathbf{k}_\alpha$  to denote the momentum obtained from  $\mathbf{k}_\alpha$  by applying the operation  $R$  on  $\mathbf{k}_\alpha$ .

<sup>1</sup> This makes sense since Lüscher's formalism also requires that exponentially suppressed corrections are negligible anyway.

Note that in the above constructions, we have not included relative orbital angular momentum of the two particles, i.e. we are only studying the  $s$ -wave scattering of the two mesons. This is justified for this particular case since close to the threshold, the scattering is always dominated by the  $s$ -wave contributions.

### B. Operators in the case of twisted boundary conditions

As explained at the end of previous section, we choose to apply twisted boundary conditions to the light quarks ( $u$  and  $d$ ) while the charm quark remains un-twisted. Single meson operators are the same as in the previous subsection except that all the operators are constructed using the primed fields. We also set the twisting angle for the  $u$  and  $d$  quark fields to be identical so that their lattice propagators are related to each other by a simple conjugation in the twisted mass formalism.

For the two-particle operators, the only difference is the discrete version of the rotational symmetry. It has been reduced from  $O_h$  to one of its subgroups:  $C_{4v}$ ,  $D_{4h}$ ,  $D_{2h}$ , or  $D_{3d}$ , depending on the particular choice of  $\theta$ . The other structures (flavor, parity when applicable etc.) of the operators remain unchanged. As a consequence, the operators  $\mathcal{P}_i$  and  $\mathcal{Q}_i$ , which used to form a basis for the  $T_1$  irrep of  $O_h$  now have to be decomposed into new basis of the corresponding subgroups [3, 15]:

$$\begin{aligned} T_1 &\mapsto A_1 \oplus E & C_{4v} , \\ T_1 &\mapsto A_2 \oplus E & D_{4h} , \\ T_1 &\mapsto B_1 \oplus B_2 \oplus B_3 & D_{2h} , \\ T_1 &\mapsto A_2 \oplus E & D_{3d} . \end{aligned} \quad (17)$$

The information for these decompositions are summarized in Table I. As an example, take the first line of Eq. (17) which corresponds to the case of  $\theta = (0, 0, \pi)$ , the original operator triplet  $(\mathcal{P}_1, \mathcal{P}_2, \mathcal{P}_3)$  should be decomposed into a singlet ( $\mathcal{P}_3$ ) and a doublet  $(\mathcal{P}_1, \mathcal{P}_2)$  which forms the basis for  $A_1$  and  $E$  irreps, respectively. Similar relations also hold for the  $\mathcal{Q}_i$ 's.<sup>2</sup>

The construction of the two-particle operators in the case of twisted boundary conditions is somewhat complex. Let us start from a general problem in group theory. Suppose that  $e_i$  form the basis of a 3-dimensional irreps  $T_1$  while  $e'_i$  form the basis of another 3-dimensional irreps  $T_1$ . With the help of group theory, the direct product of these two 3-dimensional irreps can form a 9-dimensional reducible representation of basis  $e_i \otimes e'_j (i, j = 1, 2, 3)$ . Depending on the particular choice of  $\theta$ , this new 9-dimensional reducible representation will be decomposed into irreps of the corresponding subgroup, with the linear

combinations of  $e_i \otimes e'_j (i, j = 1, 2, 3)$  giving the basis of these irreps.

To find the linear combination of basis  $e_i \otimes e'_j (i, j = 1, 2, 3)$  for definite irrep we are interested in, one could use different approaches. In our study, group character technique is used to determine the specific basis for a certain irrep.

As an application of this technique described above, taking the case of  $\theta = (\pi, \pi, 0)$  as an example, we give the corresponding operators as listed in the following equations.

$$\begin{aligned} B_1 &: e_1 \otimes e'_2 + e_2 \otimes e'_1 , \\ B_2 &: e_1 \otimes e'_3 + e_3 \otimes e'_1 , \\ B_3 &: e_2 \otimes e'_3 + e_3 \otimes e'_2 , \end{aligned} \quad (18)$$

where  $e_1 = \frac{1}{\sqrt{2}}(\mathcal{P}_1 + \mathcal{P}_2)$ ,  $e_2 = \frac{1}{\sqrt{2}}(\mathcal{P}_2 - \mathcal{P}_1)$ ,  $e_3 = \mathcal{P}_3$ . Similar relations also hold between  $e'_i$  and  $\mathcal{Q}_i$ . Then we have two-particle operators for irrep  $B_1$  as shown below:

$$\begin{aligned} \mathcal{O}^{B_1} &: \sum_{R \in G} [\mathcal{P}_2(R \circ \mathbf{k}_\alpha, t + 1) \mathcal{Q}_2(-R \circ \mathbf{k}_\alpha, t) \\ &\quad - \mathcal{P}_1(R \circ \mathbf{k}_\alpha, t + 1) \mathcal{Q}_1(-R \circ \mathbf{k}_\alpha, t)] . \end{aligned} \quad (19)$$

where  $G = D_{2h}$ , the group corresponding to  $\theta = (\pi, \pi, 0)$ .

### C. Correlation functions

For vector charmed meson  $D^*$  and  $\bar{D}^*$ , the corresponding correlation functions are defined as:

$$\begin{aligned} C^{\mathcal{P}}(\mathbf{k}, t) &= \langle \mathcal{P}_i^\dagger(\mathbf{k}, t) \mathcal{P}_i(\mathbf{k}, 0) \rangle , \\ C^{\mathcal{Q}}(\mathbf{k}, t) &= \langle \mathcal{Q}_i^\dagger(\mathbf{k}, t) \mathcal{Q}_i(\mathbf{k}, 0) \rangle , \end{aligned} \quad (20)$$

where  $\mathbf{k}$  represents the three-momentum of the relevant particle. It is straightforward to obtain the single particle energy  $E(\mathbf{k})$  for various lattice momentum  $\mathbf{k}$ . For the single particle, the dispersion relation can then be checked with various  $E(\mathbf{k})$ . In particular, this can be checked in both twisted boundary conditions and conventional periodic boundary conditions. With judicious choices of  $\theta$ , one could check the single-particle dispersion relation to a much better accuracy which will be shown in the next section.

Two-particle correlation functions are somewhat more involved. Generally speaking, a correlation matrix  $C_{\alpha\beta}^\Gamma(t)$  is constructed:

$$C_{\alpha\beta}^\Gamma(t) = \langle \mathcal{O}_\alpha^\Gamma(t) \mathcal{O}_\beta^\Gamma(0) \rangle . \quad (21)$$

where  $\mathcal{O}_\alpha^\Gamma$  represents the two-particle operator defined in the previous section and  $\Gamma$  denotes a definite irrep while  $\alpha$  enumerates different operators in that irrep. To be specific, for the non-twisted case  $\theta = (0, 0, 0)$ , the number of  $\mathbf{k}_\alpha$  is 4 in  $T_1$  channel while for all other cases, the number of  $\mathbf{k}_\alpha$  is 2. As a reference, these information are also collected in Table I.

<sup>2</sup> The reason that  $\mathcal{P}_3$  is special as opposed to  $\mathcal{P}_1$  and  $\mathcal{P}_2$  is because the twisted boundary condition with  $\theta = (0, 0, \pi)$  is applied in the 3-direction which breaks the symmetry.

TABLE I. Information about the two-particle operators used in this calculation together with the corresponding symmetries.

$\theta$	$\mathbf{0}$	$(0, 0, \frac{\pi}{2})$	$(0, 0, \pi)$	$(\pi, \pi, 0)$	$(\pi, \pi, \pi)$
Symmetry	$O_h$	$C_{4v}$	$D_{4h}$	$D_{2h}$	$D_{3d}$
irreps	$T_1$	$A_1, E$	$E$	$B_1, B_2, B_3$	$E$
Number of $\mathbf{k}_\alpha$	4	2, 2	2	2, 2, 2	2

#### IV. SIMULATION DETAILS AND RESULTS

In this paper, the Osterwalder-Seiler action [18] is used for the valence charm quark. The gauge field ensemble comes from  $N_f = 2$  twisted mass gauge field configurations generated by the European Twisted Mass Collaboration (ETMC) [9]. The gauge coupling is  $\beta = 4.05$  which corresponds to a lattice spacing of about 0.067 fm and we have used three different pion mass values, namely 300 MeV, 420 MeV and 485 MeV. Details of the relevant parameters are summarized in the Table II. The up and down bare quark mass values, characterized by the bare quark parameter  $\mu$  in Table II, are fixed to that of the sea-quark. For the charm quark, the mass parameter  $a\mu_c$  is fixed so that the value of  $\frac{1}{4}m_{\eta_c} + \frac{3}{4}m_{J/\Psi}$  calculated on the lattice reproduces the corresponding experimental value.

TABLE II. Simulation parameters in this study.

$\mu$	$N_{\text{conf}}$	$m_\pi [\text{MeV}]$	$m_\pi L$	$L^3 \times T$	$a[\text{fm}]$	$\beta$
0.003	200	300	3.3	$32^3 \times 64$	0.067	4.05
0.006	200	420	4.6	$32^3 \times 64$	0.067	4.05
0.008	200	485	5.3	$32^3 \times 64$	0.067	4.05

##### A. One-particle spectrum and dispersion relation

One-particle correlation functions as defined in Eq. (20) with definite three-momentum  $\mathbf{k}$  are calculated in our simulation from which the one-particle spectrum  $E(\mathbf{k})$  is obtained. We have checked the single particle dispersion relations for  $D^*$  and  $\bar{D}^*$  mesons, with both periodic boundary conditions and twisted boundary conditions. For the twisted boundary conditions, equivalent small momentum points offer us a more stringent test for the dispersion relation, both the continuum one and its lattice counterpart, at low-momenta close to zero. One example of these is illustrated in Fig. 1 at  $\mu = 0.003$ . The quantity  $E(\mathbf{k})^2$  or its lattice counterpart  $4\sinh^2(E/2)$  is shown versus  $p^2$  or  $\hat{\mathbf{p}}^2 = 4\sum_i \sin^2(p_i/2)$  in the bottom/top panel, respectively. The straight lines are linear fits with  $Z$  being the fitted slope of the lines.

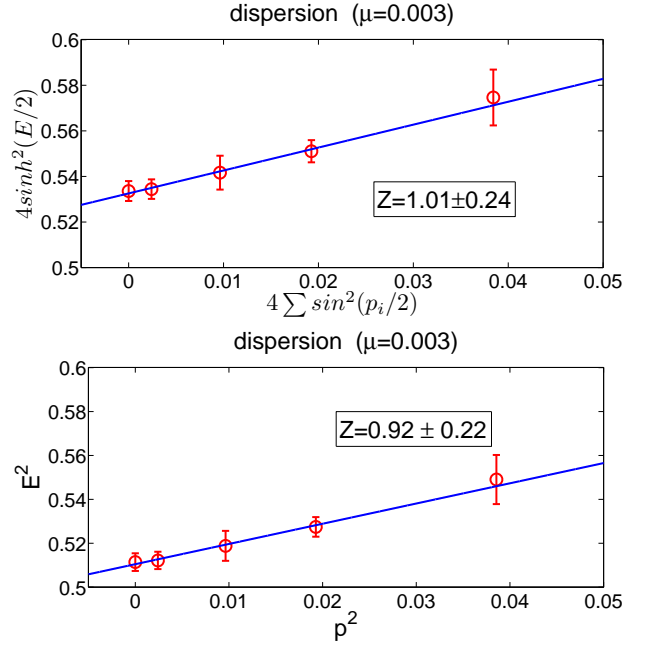


FIG. 1. Dispersion relation for the  $D^*$  meson at  $\mu = 0.003$  with lattice case (upper panel) and continuous case (lower panel). The points with error bars are lattice data while the straight lines are the corresponding linear fits with  $Z$  denoting the slope of the line.

##### B. Extraction of two-particle energy levels

In this paper, the usual Lüscher-Wolff method [19] is adopted to extract the two-particle energy eigenvalues. For this purpose, a new matrix  $\Omega(t, t_0)$  is constructed as:

$$\Omega(t, t_0) = C(t_0)^{-\frac{1}{2}} C(t) C(t_0)^{-\frac{1}{2}}, \quad (22)$$

where  $t_0$  is a reference time-slice. Normally  $t_0$  is picked such that the signal is good and stable. The energy eigenvalues for the two-particle system are then obtained by diagonalizing the matrix  $\Omega(t, t_0)$ . The eigenvalues of the matrix,  $\lambda_\alpha(t, t_0)$ , have the usual exponential decay behavior as described by  $\lambda_\alpha \sim e^{-E_\alpha(t-t_0)}$  and therefore the exact energy  $E_\alpha$  can be extracted from the effective mass plateau of the eigenvalue  $\lambda_\alpha$ .

The real signal for the eigenvalue in our simulation turns out to be somewhat noisy. To enhance the signal, the following ratio was attempted:

$$\mathcal{R}_\alpha(t, t_0) = \frac{\lambda_\alpha(t, t_0)}{C^\mathcal{P}(t-t_0, \mathbf{0}) C^\mathcal{Q}(t-t_0, \mathbf{0})} \propto e^{-\Delta E_\alpha \cdot (t-t_0)}, \quad (23)$$

where  $C^\mathcal{P}(t-t_0, \mathbf{0})$  and  $C^\mathcal{Q}(t-t_0, \mathbf{0})$  are one-particle correlation functions with zero momentum for the corresponding mesons defined in Eq. (12) and Eq. (14). Therefore,  $\Delta E_\alpha$  is the difference of the two-particle energy measured from the threshold of the two mesons:

$$\Delta E_\alpha = E_\alpha - m_{D^*} - m_{\bar{D}^*}. \quad (24)$$

The energy difference  $\Delta E_\alpha$  can be extracted from the plateau behavior of the effective mass function  $\Delta E_{\alpha,\text{eff}}(t)$  constructed from the ratio  $\mathcal{R}_\alpha(t, t_0)$  as usual:

$$\Delta E_{\alpha,\text{eff}}(t) = \ln \left( \frac{\mathcal{R}_\alpha(t, t_0)}{\mathcal{R}_\alpha(t+1, t_0)} \right). \quad (25)$$

With the energy effective energy difference  $\Delta E_{\alpha,\text{eff}}(t)$  for each time slice  $t$ , we estimate the error for each  $\Delta E_{\alpha,\text{eff}}(t)$  using the jackknife method. Then, from the effective energy difference  $\Delta E_{\alpha,\text{eff}}(t)$  and its corresponding errors, one searches a plateau in  $t$  that extends several consecutive time-slices and minimizes the  $\chi^2$  per degree of freedom. From this procedure, a fitted value of  $\Delta E_\alpha$  together with its error is obtained. As an illustration, in Fig. 2, we have shown the fitted values of  $\Delta E_\alpha$  using the jackknife method at  $\mu = 0.008$  in the  $E$  channel for  $\theta = (0, 0, \pi)$ , and the  $B_2$  channel for  $\theta = (\pi, \pi, 0)$ . As a cross check, bootstrap method is also tried to calculate the standard error of  $\Delta E_{\alpha,\text{eff}}(t)$  on each time slice. To make the comparison, the fitted values of  $\Delta E_\alpha$  are also illustrated in Fig. 3 for the same cases as in Fig. 2.

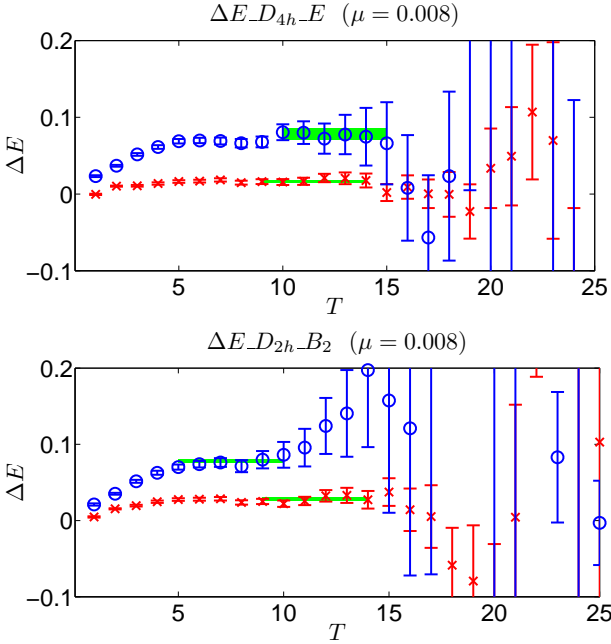


FIG. 2. Effective mass plots for the energy shift  $\Delta E_\alpha$  using the jackknife method at  $\mu = 0.008$  in the  $E$  channel for  $\theta = (0, 0, \pi)$  (top) and  $B_2$  channel for  $\theta = (\pi, \pi, 0)$  (bottom). The red crosses and the blue open circles correspond to two different energy levels obtained from Eq. (21) using  $N = 2$  different two-particle operators as discussed in the text. The horizontal bands indicate the fitted values for  $\Delta E_\alpha$  and the corresponding fitting ranges.

It is seen graphically from Fig. 2 and Fig. 3, the fitted values of  $\Delta E_\alpha$  from jackknife method is consistent with those from bootstrap method within the statistical uncertainties. The only difference is that bootstrap method seems to give a somewhat smaller error of  $\Delta E_\alpha(t)$  on each

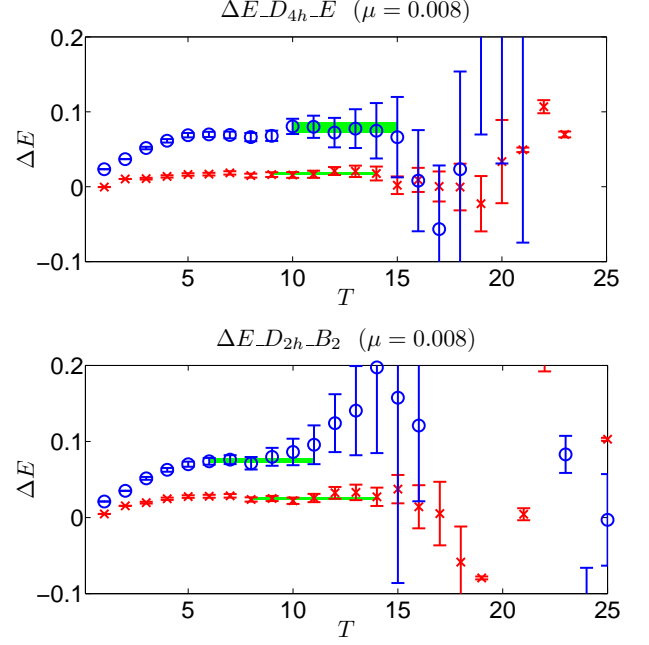


FIG. 3. Same as Fig. 2 but using the bootstrap method.

time slice. To be on the safe side, in this paper we regard the results from jackknife method as our final results for the energy levels.

Effective mass plots for other cases are similar to those shown in Fig. 2 and Fig. 3. With the energy difference  $\Delta E_\alpha$  extracted from the simulation data, one utilizes the definition:

$$\sqrt{m_{D^*}^2 + \bar{\mathbf{k}}^2} + \sqrt{m_{\bar{D}^*}^2 + \bar{\mathbf{k}}^2} = \Delta E_\alpha + m_{D^*} + m_{\bar{D}^*}. \quad (26)$$

to solve for  $\bar{\mathbf{k}}^2 \equiv (2\pi/L)^2 q^2$  which is then plugged into Lüscher's formula to obtain the information about the scattering phase shift.

The final results for  $\Delta E_\alpha$  in each irrep, together with the corresponding ranges from which the  $\Delta E_\alpha$ 's are extracted, are summarized in Table III. We only keep the two lowest energy levels for the non-twisted case and the lowest for the twisted cases, since those higher energy levels are not going to be utilized to extract the scattering parameters in the following analysis anyway.<sup>3</sup> As a result, altogether 9 energy levels are kept for the scattering analysis in the following.

### C. Extraction of scattering information

The energy considered in this study is very close to the threshold of the  $D^*-\bar{D}^*$  system, therefore one has the

<sup>3</sup> The additional operators in each particular channel helps to stabilize the lowest energy values in each irrep although the actual values of these higher states are not utilized.

$\theta$	Irrep	$\Delta E[t_{\min}, t_{\max}](\mu = 0.003)$		$\Delta E[t_{\min}, t_{\max}](\mu = 0.006)$		$\Delta E[t_{\min}, t_{\max}](\mu = 0.008)$	
		pmode0	pmode1	pmode0	pmode1	pmode0	pmode1
$\mathbf{0}$	$T_1$	0.001(2) [8,13]	0.068(3) [6,11]	0.005(2) [9,14]	0.059(4) [8,13]	0.003(1) [8,13]	0.046(3) [8,13]
$(0, 0, \frac{\pi}{2})$	$A_1$	0.001(3) [8,15]		0.012(2) [6,11]		0.007(2) [8,13]	
	$E$	0.008(2) [6,11]		0.013(1) [6,11]		0.008(2) [9,14]	
$(0, 0, \pi)$	$E$	0.004(5) [10,15]		0.019(2) [8,13]		0.017(2) [9,14]	
$(\pi, \pi, 0)$	$B_1$	0.027(3) [8,15]		0.035(3) [9,15]		0.027(1) [7,12]	
	$B_2$	0.032(3) [8,13]		0.030(3) [9,15]		0.025(2) [8,14]	
	$B_3$	0.032(2) [7,13]		0.038(2) [7,12]		0.028(2) [9,14]	
$(\pi, \pi, \pi)$	$E$	0.040(2) [5,10]		0.047(1) [5,10]		0.038(3) [7,12]	

TABLE III. Results for the energy shifts  $\Delta E$  obtained in our calculations for various cases. The time interval  $[t_{\min}, t_{\max}]$  from which we extract the values of  $\Delta E$  are also listed. These ranges are relevant for the estimation of the error for the zeta functions as described in the text.

following effective range expansion:

$$k^{2l+1} \cot \delta_l(k) = a_l^{-1} + \frac{1}{2} r_l k^2 + \dots, \quad (27)$$

where  $a_l$  is the so-called scattering length for partial wave  $l$  and  $r_l$  is the corresponding effective force range while  $\dots$  represents terms that are higher order in  $k^2$ . It is more convenient to use a dimensionless form in our analysis. With  $q^2 = k^2 L^2 / (2\pi)^2$ , Eq. (27) can be rewritten in terms of  $q^2$ :

$$q^{2l+1} \cot \delta_l(q^2) = B_l + \frac{1}{2} R_l q^2 + \dots, \quad (28)$$

with  $B_l = [L/(2\pi)]^{2l+1} a_l^{-1}$  and  $R_l = [L/(2\pi)]^{2l-1} r_l$ . In the following, we will call parameters  $B_l$  and  $R_l$  the low-energy scattering parameters in partial wave  $l$  and our task is to extract these parameters from our simulation data. Since we have a definite lattice size and lattice spacing, it turns out that  $q^2 \simeq 1$  corresponds to  $k^2 \simeq [580 \text{ MeV}]^2$  in physical units.

It is also well-known that, close to the threshold, scattering is dominated by phase shifts coming from lower partial waves as long as they are non-vanishing. Therefore all partial waves with  $l \geq 2$  will be ignored in the Lüscher formula for this study. As mentioned in previous section, the irreps studied in this paper all preserve parity except for the case of  $\theta = (0, 0, \pi/2)$  which breaks parity. Using the terminology in Ref. [3], this is the only parity-mixing scenario while all other points belong to the parity-conserving scenario. Thus to extract these low-energy scattering parameters from the lattice data, we have altogether 9 points for different  $q^2$  values: 2 points in the parity-mixing case with  $\theta = (0, 0, \pi/2)$  and 7 points in the parity-conserving case. These are all tabulated in Table III.

As all contributions from  $l \geq 2$  partial waves have been neglected, the parity-conserving data (7 points) will depend only on the  $s$ -wave parameters  $B_0$  and  $R_0$  while the parity-mixing data (2 points) will depend on both the  $s$ -wave parameters and the  $p$ -wave parameters  $B_1$  and  $R_1$ . There are 3 different strategies to follow here:

1. A combined correlated fit using all 9 data points.

This yields the low-energy scattering parameters for both  $s$ -wave and  $p$ -wave;

2. A correlated fit using only the parity-conserving points. This yields only the  $s$ -wave low-energy scattering parameters.
3. A correlated fit using all data points, neglecting the parity-mixing effects of the two data points for  $\theta = (0, 0, \pi/2)$ . This also only yields the  $s$ -wave scattering parameters.

We will first describe the fitting process following strategy 1 listed above. The other strategies follow similarly and the results will also be listed for comparisons.

To be specific, in the parity-conserving case, we define

$$y_0(q^2) = m_{00}(q^2). \quad (29)$$

According to Lüscher's formula Eq. (5), this should be equal to

$$q \cot \delta_0(q^2) = m_{00}(q^2) = \frac{1}{\pi^{3/2}} \mathcal{Z}_{00}(1; q^2), \quad (30)$$

for the non-twisted case while for the twisted case, one simply replace the corresponding zeta function by  $\mathcal{Z}_{00}^\theta(1; q^2)$  [15]. In the parity-mixing case, however, things are more complicated. Apart from the  $s$ -wave phase shift  $\delta_0(q^2)$ , Lüscher formula will also involve  $\delta_1(q^2)$ . Accordingly, we define

$$y_1(q^2) = [m_{01}(q^2)]^2, \quad (31)$$

and, according to Lüscher's formula, it is equal to

$$y_1(q^2) = [q \cot \delta_0(q^2) - m_{00}][q \cot \delta_1(q^2) - m_{11}] \quad (32)$$

where the functions  $m_{00}$ ,  $m_{01}$  and  $m_{11}$  are related to the corresponding zeta-functions, see e.g. Ref. [15].

For definiteness, we label the data points as follows: the parity-conserving data points are labelled from 1 to  $N_0 = 7$  while the parity-mixing points are labelled from  $N_0 + 1 = 8$  to  $N_0 + N_1 = 7 + 2 = 9$ . For later convenience, we also introduce an index function as follows,

$$\text{ind}(I) = \begin{cases} 0 & \text{for } 1 \leq I \leq N_0 \\ 1 & \text{for } N_0 + 1 \leq I \leq N_0 + N_1 \end{cases} \quad (33)$$

In other words,  $ind(I) = 0$  for the first  $N_0$  parity-conserving data points while  $ind(I) = 1$  for the next  $N_1$  parity-mixing data points. So our previous definitions of  $y_0(q^2)$  and  $y_1(q^2)$  may be written collectively as  $y_{ind(I)}(q_I^2)$  with  $I = 1, 2, \dots, (N_0 + N_1)$ . We can then construct the  $\chi^2$  function as usual

$$\chi^2 = \sum_{I,J=1}^{N_0+N_1} [F_{ind(I)}(q_I^2; \alpha) - y_{ind(I)}(q_I^2)] C_{IJ}^{-1} [F_{ind(J)}(q_J^2; \alpha) - y_{ind(J)}(q_J^2)] \quad (34)$$

where for  $ind(I) = 0, 1$  the corresponding functions are (using the symbol  $\alpha$  to collectively denote all the relevant fitting parameters  $B_0$ ,  $R_0$ ,  $B_1$  and  $R_1$ ):

$$F_0(q^2; \alpha) = B_0 + \frac{R_0}{2} q^2, \quad (35)$$

$$F_1(q^2; \alpha) = [B_0 + \frac{R_0}{2} q^2 - m_{00}][B_1 + \frac{R_1}{2} q^2 - m_{11}]. \quad (36)$$

For the estimation of the covariance matrix  $C_{IJ}$  and also the errors for the zeta-functions that appear in the above formulas, we closely follow the steps outlined in Ref. [3]. The reader is referred to that reference for further details. Basically, minimizing the target  $\chi^2$  function in Eq. (34), one could obtain all the parameters, namely  $B_0$ ,  $R_0$ ,  $B_1$  and  $R_1$ , in a single step with all of our data. In the course of inverting the covariance matrix  $C$  in Eq. 34, the eigenvalues of the covariance matrix for each irrep have been calculated with both QR decomposition and singular value decomposition. The corresponding results show that the matrices are nonsingular.

To get a feeling of these fits, we plot the quantity  $q \cot \delta_0(q^2)$  vs.  $q^2$  in Fig. 4 obtained from strategy 1. The values of  $q \cot \delta_0(q^2)$  for the data points are obtained via the relation

$$q \cot \delta_0(q^2) = m_{00} + \frac{m_{01}^2}{q^3 \cot \delta_1(q^2) - m_{11}}, \quad (37)$$

where the quantity  $q^3 \cot \delta_1(q^2)$  on the r.h.s of the above equation is replaced by  $B_1 + \frac{1}{2} R_1 q^2$  with the fitted values for  $B_1$  and  $R_1$ . This figure illustrates the situation for all three pion masses in our simulation. From top to bottom, each panel corresponds to  $\mu = 0.003$ ,  $\mu = 0.006$  and  $\mu = 0.008$ , respectively. All data points obtained from our simulation are plotted in these figures. The blue open circles are the data points in the parity-conserving cases while the two red crosses in each panel are the data for the parity-mixing case. The straight lines in the figure illustrates the fitting function  $F_0(q^2; \alpha) = B_0 + (R_0/2)q^2$  and the shaded bands indicate the corresponding uncertainties. As is seen from the figure, we do get a reasonable fit for all three pion mass values. Finally, the fitted values for the scattering parameters are summarized in Table IV for three values of  $m_\pi^2$  in our simulation.

To check the validity of the effective range expansion, we may also compare the  $s$ -wave phase shift  $\delta_0(q^2)$  itself

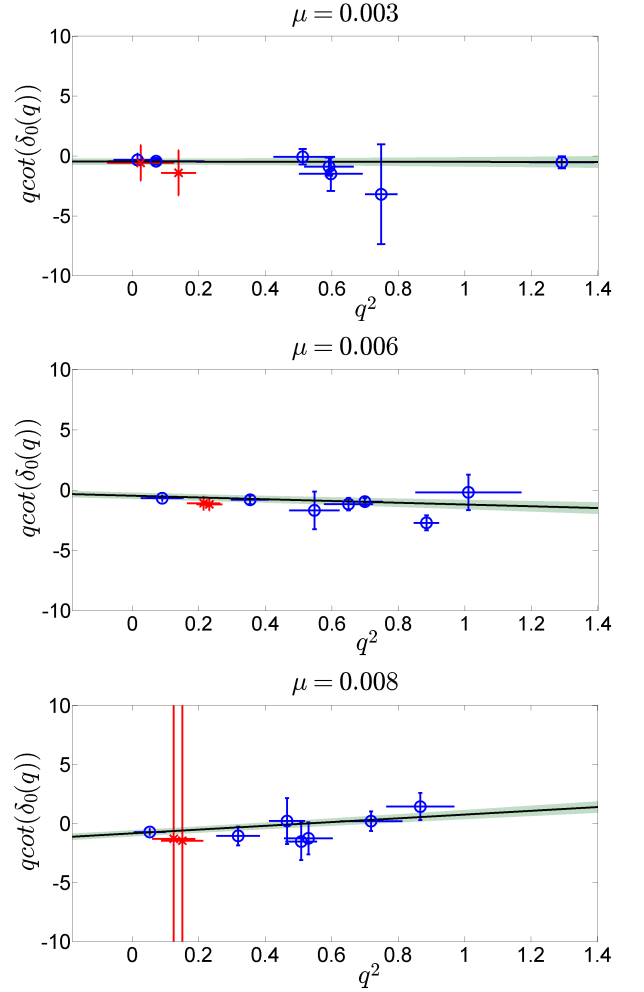


FIG. 4. Results for the correlated fits from strategy 1 as described in the text. Each panel, from top to bottom, corresponds to  $\mu = 0.003, 0.006$  and  $0.008$ , respectively. The quantity  $q \cot \delta_0(q^2)$  is plotted versus  $q^2$  for all our data points, both parity-conserving case (blue open circles) and parity-mixing case (red crosses). The straight lines indicates the fitted result for  $q \cot \delta_0(q^2) = B_0 + (R_0/2)q^2$  and the shaded bands indicates the corresponding uncertainties.

$\mu$	$B_0$	$R_0$	$B_1$	$R_1$	$\chi^2/dof$
0.003	-0.47(35)	-0.051(243)	0.32(17)	-9.15(2.46)	1.66/5
0.006	-0.46(23)	-1.46(1.38)	-0.14(05)	-0.59(32)	9.92/5
0.008	-0.83(17)	3.18(2.12)	0.85(31)	-14.42(5.83)	3.52/5

TABLE IV. Fit results with strategy 1.

$\mu$	$B_0$	$R_0$	$\chi^2/dof$
0.003	-0.42(38)	-0.13(43)	1.62/5
0.006	-0.47(19)	-1.45(1.16)	9.92/5
0.008	-0.84(13)	3.18(2.29)	3.52/5

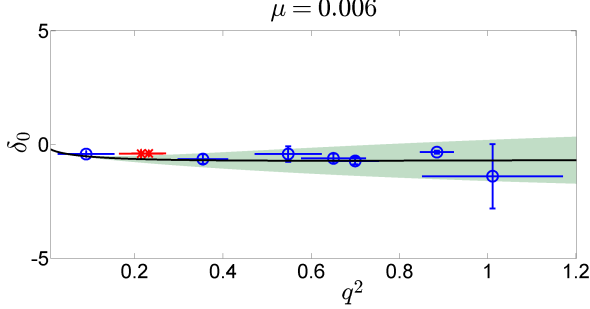
TABLE V. Fit results with strategy 2.

as a function  $q^2$ . The situation is shown in FIG. 5 for



$\mu$	$B_0$	$R_0$	$\chi^2/dof$
0.003	-0.57(27)	0.15(59)	2.44/7
0.006	-0.33(21)	-1.72(1.25)	10.94/7
0.008	-0.61(3)	2.94(2.58)	5.04/7

TABLE VI. Fit results with strategy 3.

FIG. 5. The same as Fig. 4, but the comparison is done for the  $s$ -wave phase shift  $\delta_0(q^2)$  itself. This is the case of  $\mu = 0.006$ .

$\mu = 0.006$ .

Similarly, one could follow strategy 2 listed above and obtain the  $s$ -wave parameters using only the parity-conserving data points, i.e. the first 7 data points. Or, alternatively following strategy 3 and obtain the  $s$ -wave scattering parameters using all the data points by neglecting the mixing between the  $s$ -wave and  $p$ -wave. Numerically this amounts to setting the matrix elements  $m_{01} = 0$  compared with the diagonal ones. The results obtained from these strategies can be compared with what we get from strategy 1. It turns out that, the mixing of the  $s$ - and  $p$ -wave indeed has little impact on the final results for the  $s$ -wave scattering parameters. The corresponding fitted results are summarized in Table V and Table VI, respectively.

As is seen from these tables, as far as the  $s$ -wave scattering parameters are concerned, it seems that the parity-conserving data dominate the final fitting results. This is illustrated by consistent values for  $B_0$  and  $R_0$  in Table IV and Table V. Finally, we regard our correlated fits from strategy 1 with all of our data as being more reliable and they are taken as our final results for this paper.

#### D. Physical values for the scattering parameters

The relation between the fitted values of  $B_l$ ,  $R_l$  for  $l = 0, 1$  and scattering parameters can be expressed as follows:

$$a_l = \left(\frac{L}{2\pi}\right)^{2l+1} \left(\frac{1}{B_l}\right), \quad r_l = R_l \left(\frac{2\pi}{L}\right)^{2l-1}. \quad (38)$$

Taking the numbers of correlated fitting in Table IV, for the  $s$ -wave, we can obtain the scattering length  $a_0$ :

$-0.72(54)\text{fm}$ ,  $-0.74(37)\text{fm}$ ,  $-0.41(8)\text{fm}$  for  $\mu = 0.003$ ,  $0.006$ ,  $0.008$ , respectively. The values for  $r_0$  can be also obtained accordingly. These numbers are summarized in Table VII.

From strategy 2 and strategy 3, the correlated fitting are also conducted to obtain the scattering length  $a_0$  and effective force range  $r_0$ . The specific results are summarized in Table VIII and Table IX, respectively.

	$\mu = 0.003$	$\mu = 0.006$	$\mu = 0.008$
$a_0[\text{fm}]$	-0.72(54)	-0.74(37)	-0.41(8)
$r_0[\text{fm}]$	-0.018(83)	-0.50(43)	1.08(73)

TABLE VII. The values for  $a_0$  and  $r_0$  in physical units obtained from the numbers for the correlated fit in Table IV, from strategy 1.

	$\mu = 0.003$	$\mu = 0.006$	$\mu = 0.008$
$a_0[\text{fm}]$	-0.80(71)	-0.73(30)	-0.41(6)
$r_0[\text{fm}]$	-0.043(146)	-0.49(46)	1.09(78)

TABLE VIII. The values for  $a_0$  and  $r_0$  in physical units obtained from the numbers for the correlated fit in Table V, from strategy 2.

	$\mu = 0.003$	$\mu = 0.006$	$\mu = 0.008$
$a_0[\text{fm}]$	-0.60(28)	-1.03(65)	-0.56(3)
$r_0[\text{fm}]$	0.05(20)	-0.59(43)	1.00(88)

TABLE IX. The values for  $a_0$  and  $r_0$  in physical units obtained from the numbers for the correlated fit in Table VI, from strategy 3.

#### E. Scattering parameters using the bootstrap method

The errors used in the analysis discussed so far are estimated using the jackknife method. To crosscheck these results, bootstrap method is also utilized to analyze directly the final scattering length  $a_0$  and effective range  $r_0$ . The specific procedure is as follows.

1. Select randomly 200 configurations from the given configurations in Table II for each parameter  $\mu$ . Do the selection  $N_{\text{random}}$  times and label each sample by an integer  $i$ ,  $i = 1, 2, \dots, N_{\text{random}}$ .
2. For each randomly selected sample  $i$ , repeat the analysis process described so far in section IV. This yields one set of scattering parameters, say  $1/a_0^i$  and  $r_0^i$ .
3. Analyze the distribution of these values. Taking  $r_0$  as an example, find the values  $p$  and  $q$  so that these

bracket the central 68% of the  $r_0^i$  values:

$$\frac{N(r_0^i < p)}{N_{random}} = 0.16 \quad \frac{N(r_0^i > q)}{N_{random}} = 0.16 \quad (39)$$

where  $N(r_0 < p)$  denotes the number of  $r_0^i$  satisfying  $r_0^i < p$ .

- the bootstrap estimate of the asymmetric errors for the quantity can be given as:

$$r_0 = \langle r_0 \rangle_{-(\langle r_0 \rangle - p)}^{+(q - \langle r_0 \rangle)} \quad (40)$$

with  $\langle r_0 \rangle$  denoting the weighted mean of  $\{r_0^i\}$ .

In this work, we take  $N_{random} = 60$  at three different  $\mu$  ( $\mu = 0.003, 0.006, 0.008$ ) to estimate the bootstrap error of scattering parameters with strategy 2 described in section IV. As an illustration, the distribution of  $1/a_0^i$  and  $r_0^i$  for case  $\mu = 0.003$  are shown in FIG. 6. Meanwhile, the asymmetric error of  $a_0$  and  $r_0$  are estimated with these 60 samples. These final specific values are summarized in Table X.

Alternatively, we have also estimated the bootstrap error of scattering parameters with strategy 3. The only difference is that the data points corresponding to  $A_1$  and  $E$  irreps ( $\theta = (0, 0, \pi/2)$ ) are not left out during the process, that is neglecting the parity-mixing of effects of the two data points. The final results are summarized in Table XI.

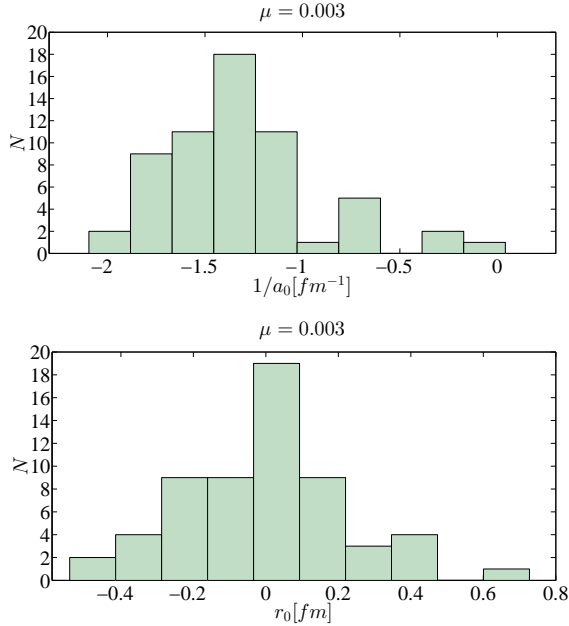


FIG. 6. Distribution of  $\{1/a_0^i\}$  and  $\{r_0^i\}$  from strategy 3 for bootstrap method at  $\mu = 0.003$ .

As observed from Table IX, Table VIII, Table XI, and Table X, jackknife method and bootstrap method yield compatible results.

	$\mu = 0.003$	$\mu = 0.006$	$\mu = 0.008$
$a_0[\text{fm}]$	$-0.74^{+0.21}_{-0.15}$	$-0.68^{+0.19}_{-0.18}$	$-0.48^{+0.22}_{-0.22}$
$r_0[\text{fm}]$	$-0.0048^{+0.18}_{-0.20}$	$-0.038^{+0.12}_{-0.16}$	$0.73^{+0.58}_{-0.62}$

TABLE X. The values for  $a_0$  and  $r_0$  from strategy 2 with parity-conserving data points with bootstrap method at  $\mu = 0.003, 0.006, 0.008$ .

	$\mu = 0.003$	$\mu = 0.006$	$\mu = 0.008$
$a_0[\text{fm}]$	$-0.76^{+0.14}_{-0.21}$	$-0.86^{+0.22}_{-0.22}$	$-0.59^{+0.19}_{-0.25}$
$r_0[\text{fm}]$	$-0.0022^{+0.18}_{-0.19}$	$-0.14^{+0.15}_{-0.18}$	$0.64^{+0.50}_{-0.51}$

TABLE XI. The values for  $a_0$  and  $r_0$  from strategy 3 with all data points with bootstrap method at  $\mu = 0.003, 0.006, 0.008$ .

## F. Implication of our results

As is said, we take the fitted result from strategy 1 as our final results, i.e. those in Table IV and Table VII. Based on our results, the values of  $a_0$  do not seem to follow a regular chiral extrapolation pattern, at least not within the range that we have studied. We therefore kept the individual values for  $a_0$  and  $r_0$  for each case. This irregularity might be caused by the smallness of the value  $m_\pi L \sim 3.3$  for  $\mu = 0.003$ . To circumvent this, one has to study a larger lattice.

The negative values of the parameter  $B_0$  (hence the scattering length  $a_0$ ) indicates that the two constituent mesons for the  $(D^* \bar{D}^*)^\pm$  system have weak repulsive interactions at low energies. Therefore, our result does not support the bound state scenario for these two mesons.

Another check for the possible bound state would be to look for those negative  $q^2$  values we obtained which corresponds to the negative values of  $\delta E$  listed in Table III. However, the  $q^2$  for different channel in our study are all positive which contradicts the possibility of a bound state. Since the cases we are studying is still far from the physical pion mass case, we still cannot rule out the possibility the appearance of a bound state once the pion mass is lowered (and the lattice size  $L$  is also increased accordingly to control the finite volume corrections). Such scenarios do occur in lattice studies of two nucleons.

## V. CONCLUSIONS

In this paper, the low-energy scattering of  $D^*$  and  $\bar{D}^*$  is studied with  $N_f = 2$  twisted mass fermion configurations. In our calculation, three different pion mass values ( $m_\pi = 300, 420, 485$  MeV) are utilized to investigate the pion mass dependence, and the corresponding lattice size is  $32^3 \times 64$  with a lattice spacing  $a \simeq 0.067$  fm. We have used twisted boundary conditions to enhance the momentum resolution close to the threshold. Using Lüscher's

finite-size technique, the  $s$ -wave scattering in the channel  $J^P = 1^+$  is studied and the scattering parameters are obtained by correlated fitting procedure. As a cross-check, two different statistical error estimating methods, jackknife and bootstrap method are utilized which yield compatible results for the  $s$ -wave scattering parameters. The results from a correlated fit with all of the data with errors estimated using the jackknife method is regarded as the final result for this paper.

Our results indicate that, for all three pion mass values that we simulated, the scattering lengths are negative which indicates a weak repulsive interaction between the two mesons ( $D^*$  and  $\bar{D}^*$  or its conjugated systems under  $C$ -parity or  $G$ -parity). Thus a bound state of the two mesons in  $J^P = 1^+$  channel is not supported based on our current lattice results. However, as we pointed out already, we cannot rule out the possibility of a bound state for the two vector charmed mesons when the pion mass is lowered and the volume is increased accordingly. This requires further systematic lattice studies. Furthermore, it is also possible that more complete set of interpolation operators and a coupled channel study is required. In summary, this lattice study has shed some light on the

nature of  $Z_c^\pm(4025)$  however it remains to be clarified by future more systematic studies.

## ACKNOWLEDGEMENTS

The authors would like to thank F. K. Guo, B. Knippschild, L. Liu, U. Meissner, A. Rusetsky, and C. Urbach for helpful discussions. The authors would like to thank the European Twisted Mass Collaboration (ETMC) to allow us to use their gauge field configurations. Our thanks also go to National Supercomputing Center in Tianjin (NSCC) and the Beijing Computing Center (BCC) where part of the numerical computations are performed. This work is supported in part by the National Science Foundation of China (NSFC) under the project No.11335001, No.11275169, No.11075167, No.11105153. It is also supported in part by the DFG and the NSFC (No.11261130311) through funds provided to the Sino-German CRC 110 “Symmetries and the Emergence of Structure in QCD”. M. Gong and Z. Liu are partially supported by the Youth Innovation Promotion Association of CAS (2013013, 2011013).

- 
- [1] M. Ablikim et al. (BESIII Collaboration), Phys.Rev.Lett. **110**, 252001 (2013), arXiv:1303.5949 [hep-ex].
  - [2] M. Ablikim et al. (BESIII Collaboration), Phys.Rev.Lett. **112**, 132001 (2014), arXiv:1308.2760 [hep-ex].
  - [3] W. Chen, T. Steele, M.-L. Du, and S.-L. Zhu, Eur.Phys.J. **C74**, 2773 (2014), arXiv:1308.5060 [hep-ph].
  - [4] J. He, X. Liu, Z.-F. Sun, and S.-L. Zhu, Eur.Phys.J. **C73**, 2635 (2013), arXiv:1308.2999 [hep-ph].
  - [5] C.-F. Qiao and L. Tang, Eur.Phys.J. **C74**, 2810 (2014), arXiv:1308.3439 [hep-ph].
  - [6] C.-Y. Cui, Y.-L. Liu, and M.-Q. Huang, Eur.Phys.J. **C73**, 2661 (2013).
  - [7] S. Prelovsek, C. Lang, L. Leskovec, and D. Mohler, Phys.Rev. **D91**, 014504 (2015), arXiv:1405.7623 [hep-lat].
  - [8] Y. Chen, M. Gong, Y.-H. Lei, N. Li, J. Liang, et al., Phys.Rev. **D89**, 094506 (2014), arXiv:1403.1318 [hep-lat].
  - [9] B. Blossier et al. (ETM Collaboration), Phys.Rev. **D82**, 114513 (2010), arXiv:1010.3659 [hep-lat].
  - [10] M. Luscher, Nucl.Phys. **B354**, 531 (1991).
  - [11] S. Prelovsek, L. Leskovec, and D. Mohler, (2013), arXiv:1310.8127 [hep-lat].
  - [12] S. Sasaki and T. Yamazaki, PoS **LAT2007**, 131 (2007), arXiv:0709.1002 [hep-lat].
  - [13] P. F. Bedaque, Phys.Lett. **B593**, 82 (2004), arXiv:nucl-th/0402051 [nucl-th].
  - [14] C. Sachrajda and G. Villadoro, Phys.Lett. **B609**, 73 (2005), arXiv:hep-lat/0411033 [hep-lat].
  - [15] S. Ozaki and S. Sasaki, Phys.Rev. **D87**, 014506 (2013), arXiv:1211.5512 [hep-lat].
  - [16] D. Agadjanov, U.-G. Meissner, and A. Rusetsky, JHEP **1401**, 103 (2014), arXiv:1310.7183 [hep-lat].
  - [17] G.-Z. Meng et al. (CLQCD Collaboration), Phys.Rev. **D80**, 034503 (2009), arXiv:0905.0752 [hep-lat].
  - [18] R. Frezzotti and G. Rossi, JHEP **0410**, 070 (2004), arXiv:hep-lat/0407002 [hep-lat].
  - [19] M. Luscher and U. Wolff, Nucl.Phys. **B339**, 222 (1990).